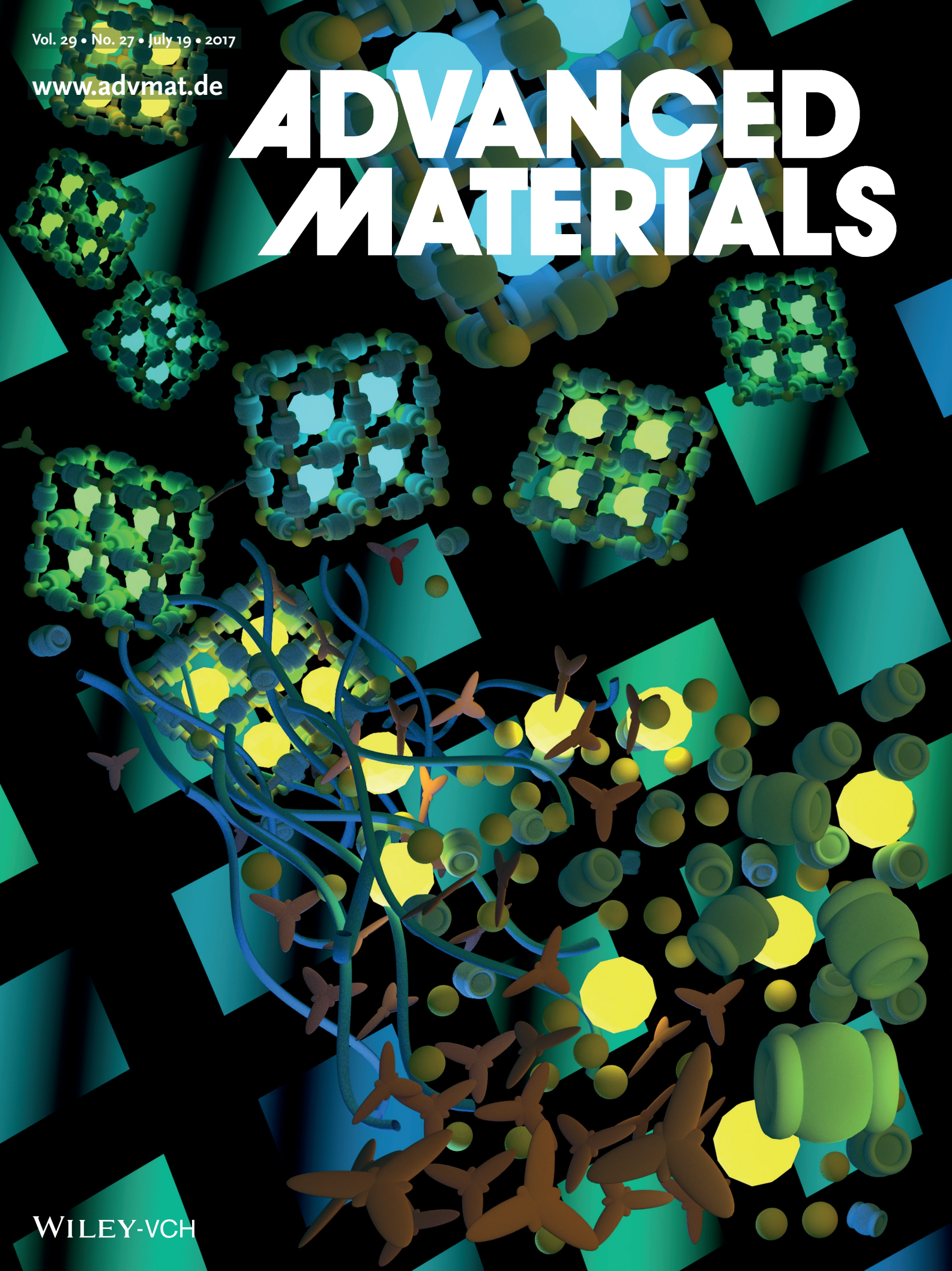


Vol. 29 • No. 27 • July 19 • 2017

www.advmat.de

ADVANCED MATERIALS



WILEY-VCH

Optochemically Responsive 2D Nanosheets of a 3D Metal–Organic Framework Material

Abhijeet K. Chaudhari, Ha Jin Kim, Intaek Han, and Jin-Chong Tan*

Outstanding functional tunability underpinning metal–organic framework (MOF) confers a versatile platform to contrive next-generation chemical sensors, optoelectronics, energy harvesters, and converters. A rare exemplar of a porous 2D nanosheet material constructed from an extended 3D MOF structure is reported. A rapid supramolecular self-assembly methodology at ambient conditions to synthesize readily exfoliatable MOF nanosheets, functionalized in situ by adopting the guest@MOF (host) strategy, is developed. Nanoscale confinement of light-emitting molecules (as functional guest) inside the MOF pores generates unusual combination of optical, electronic, and chemical properties, arising from the strong host–guest coupling effects. Highly promising photonics-based chemical sensing opened up by the new guest@MOF composite systems is shown. By harnessing host–guest optochemical interactions of functionalized MOF nanosheets, detection of an extensive range of volatile organic compounds and small molecules important for many practical applications has been accomplished.

2D nanosheets are contemporary materials with exceptional physical and functional properties, derived from a broad class of low-dimensional solids containing atomically thin structures,^[1] exfoliated 2D frameworks,^[2] and molecular membranes.^[3] Considerable efforts are being devoted to 2D graphene-related materials^[4] to yield improved mechanical, electronic, and optical modulations, important for device integration and disruptive technologies. On the contrary, far less widespread are thin-layered materials derived from self-assembled supramolecular systems,^[5] whose weak interlayer noncovalent chemical interactions are van der Waals in nature. Such molecule-based 2D materials may provide significant benefits toward physical and

chemical tunability, structural flexibility, and ease of exfoliation.^[6] There is recent intensifying interest in an emergent class of 2D nanosheets constructed by downsizing 3D metal–organic frameworks (MOFs),^[3a,7] which are inorganic–organic (hybrid) structures possessing an enormous physicochemical^[8] and structural versatility.^[9] Furthermore, the nanoscale porosity of MOFs could function as a vessel to “host” a variety of functional “guest” molecules,^[10] imparting a unique combination of properties through intimate host–guest interactions.^[11] Yet, preparation of a functionalized MOF as 2D nanosheets exemplifying a tunable host–guest sensing response is uncommon in literature, unlike its traditional counterparts.^[12]

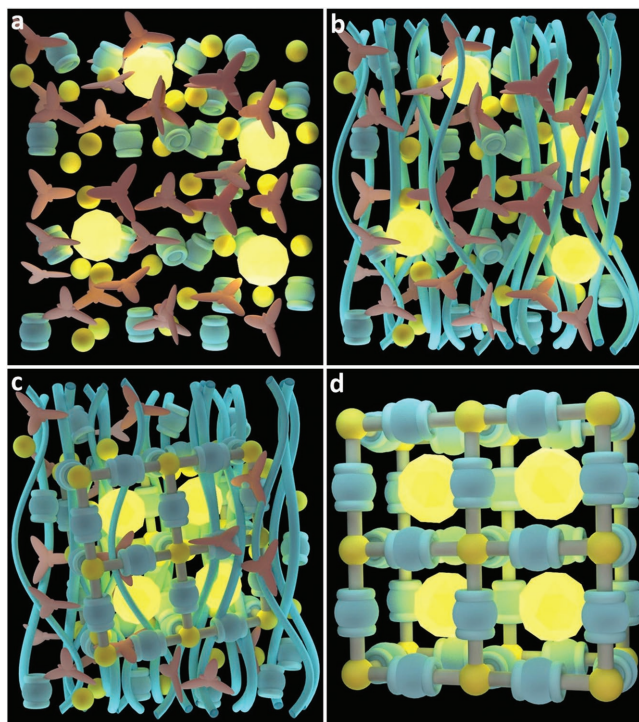
In this work, we present a simple supramolecular self-assembly strategy to accomplish concomitant 2D nanosheet synthesis and functionalization of a porous MOF system, and demonstrate its efficacy for application as a tunable optochemical sensor. We leverage our recently elucidated supramolecular “high-concentration reactions” (HCR) approach,^[13] to realize one-pot synthesis of functionalized MOF nanosheets at ambient conditions; the basic concept is illustrated in **Scheme 1**. Here we describe a representative study employing 1,4-benzenedicarboxylic acid (BDC) as the organic linker, because of its strong propensity to construct an extended chemical network upon coordination with metal centers; for instance, here we utilized divalent Zn²⁺. Triethylamine base (NEt₃) featuring a flexible tripodal geometry was used to trigger fast activation (deprotonation) of the BDC linkers.^[14] It is striking to see that, a white gel-like fibrous soft matter was immediately obtained at room temperature (**Figure 1a**), arising from the HCR between Zn²⁺ and BDC²⁻, augmented by the NEt₃⁺ cations. We observed a discernible two-stage material transformation via optical microscopy (**Figure 1b**): initially witnessing development of highly oriented fibers, prior to formation of a visually *shiny* phase prevalent on the fiber surfaces. The gel fiber diameter was found to be ≈1–10s μm by scanning electron microscopy (SEM), see **Figure 1c**. Intriguingly, SEM revealed those supramolecular fibers are, in fact, constituting densely packed crystalline nanosheets (**Figure 1d**), thus confirming the (shiny) faceted appearance detected under optical microscopy (**Figure 1b**). To establish the detailed 2D morphologies, we examined nanosheets harvested from the supramolecular gels using transmission electron microscopy (TEM) and SEM (**Figure 1e,f**), as well as by atomic force microscopy (AFM) with which we have estimated the nominal thickness of

A. K. Chaudhari, Prof. J.-C. Tan
Multifunctional Materials & Composites (MMC) Laboratory
Department of Engineering Science
University of Oxford
OX1 3PJ Oxford, UK
E-mail: jin-chong.tan@eng.ox.ac.uk

Dr. H. J. Kim, Dr. I. T. Han
Materials Research Center, Samsung Advanced Institute
of Technology (SAIT)
Samsung Electronics Co. Ltd.
443-803 Suwon, Republic of Korea

This is an open access article under the terms of the Creative Commons Attribution License, which permits use, distribution and reproduction in any medium, provided the original work is properly cited.
The copyright line for this article was changed on 23 May 2017 after original online publication.

DOI: 10.1002/adma.201701463



Scheme 1. Proposed supramolecular synthetic strategy for constructing an optochemically active guest@MOF (host) system. a) In situ assembly began with a one-pot solution mixture of high-concentration reactants, combined with functional guest species (e.g., luminescent complexes represented by yellow spheres). b) This solution mixture produces a fibrous supramolecular assembly, facilitating formation of c) periodic MOF structures encapsulating functional guest molecules. d) Disassembly of scaffolding fibers to harvest functionalized guest@MOF composite systems.

the exfoliated 2D sheets is of the order of 10s nm (Figure 1g). Additional microscopy images showing the 2D nanosheet morphologies are presented in the Supporting Information, see Figures S1–S12 (Supporting Information).

Powder X-ray diffraction studies (PXRD) (Figure 2a,b) of nanosheets extracted from the supramolecular fibers (Figure 1e,f) showed crystallographic resemblance to a 3D MOF structure: $(\text{H}_2\text{NEt}_2)_2[\text{Zn}_3\text{BDC}_4] \cdot 3\text{DEF}$ reported by Burrows et al.^[15] and Stock and co-workers.^[16] However, there are important differences between the present MOF nanosheets and the materials mentioned earlier, from both the structural and the synthetic points of view. First, our diffraction data evidenced strong signature of peak shifts, especially of the diagonal (110) planes (Figure 2b), which we solved by Pawley refinement^[17] (Figure 2a) revealing salient variations in the basic unit cell geometry (triclinic vs monoclinic, see Table S1, Supporting Information); and there are substantial peak broadening arising from the fine-scale nanosheet morphology. Crucially the crystal structure has predominantly unidirectional pores (Figure 2c), comprising 1D undulating channels down the *c*-axis. Second, neutralization of the framework negative charges was previously mediated by diethylammonium cations (H_2NEt_2^+) liberated from hydrolysis of *N,N*-diethylformamide (DEF) solvent, accomplished either in a strong acidic solution (2 M HNO_3) at high-temperature synthesis (120 °C, 1 d),^[16] or, in the presence of water molecules under protracted conditions (approximately

weeks).^[15] In contrast, MOF nanosheets prepared via our rapid HCR method at room temperature (less than 1 min) incorporate charge-balancing cations NEt_3^+ (derived from its neutral form, when activating BDC linkers). Considered together our results show that, inclusion of NEt_3^+ cations inside MOF pores leads to deformation of host framework, where structural distortion by straining has reduced unit cell symmetry (Table S1, Supporting Information). We subsequently established the chemical formula of the present MOF structure to be: $(\text{HNEt}_3)_2[\text{Zn}_3\text{BDC}_4] \cdot \text{solvent}$ where *solvent* = DMF or DMA (vide infra), validated by thermogravimetric analysis (TGA) (Figures S16 and S17, Supporting Information). Hereafter the identified MOF nanosheet structure is designated as “OX-1” (i.e., Oxford University-1 material).

Remarkably our HCR strategy can be adopted, to directly functionalize OX-1 nanosheets to derive new photoactive “guest@host” composite systems. To illustrate this, we demonstrate in situ nanoscale confinement of the luminescent metal complex “guest” molecule: zinc(II) bis(8-hydroxyquinoline),^[18] termed ZnQ, spatially confined inside the 1D pore channels of the OX-1 “host” framework employing one-pot supramolecular synthesis.^[14] We discovered that, the coupled guest@host systems synthesized from *N,N*-dimethylformamide (DMF) and *N,N*-dimethylacetamide (DMA) solvents displayed significantly different luminescent behavior, although identical synthetic conditions^[14] were applied, other than their solvent type. When subjected to UV irradiation it can be seen that nanosheets synthesized in DMF solvent emit an intense blue light ($\lambda_{\text{em}} = 470$ nm) (Figure 2d), whereas samples from DMA solvent display a green light emission ($\lambda_{\text{em}} = 510$ nm). Henceforth, we designate these two new guest@host nanosheet systems as: $\text{ZnQ}_{\text{DMF}}@OX-1$ and $\text{ZnQ}_{\text{DMA}}@OX-1$, respectively (subscript denotes solvent type used in synthesis). To understand their differential structure–property relationships, we performed spectroscopic measurements to study the detailed photophysical properties.

Absorption UV–vis spectroscopic measurements were used to elucidate the nature of the host–guest interactions and to identify spatial confinement effects due to nanoscale porosity. It can be seen in Figure 2e that, functionalized nanosheets of $\text{ZnQ}_{\text{DMF}}@OX-1$ and $\text{ZnQ}_{\text{DMA}}@OX-1$ exhibit an appreciably enhanced π – π^* electronic transition at 291 nm, confirming the successful encapsulation of luminous ZnQ guest emitter within the pores of the OX-1 host framework. This energy transfer phenomenon is caused by close-packing of host–guest aromatic moieties, characteristic of the caged guest molecules. Figure 2f shows the modification of band gaps as a consequence of intimate host–guest coupling. Through encapsulation of ZnQ in the OX-1 pores we have evidenced a clear reduction in the band gap of the OX-1 framework, which fell from greater than 4 eV to just below 2.8 eV. Interestingly, we found that $\text{ZnQ}_{\text{DMA}}@OX-1$ exhibits a maximum absorption corresponding to the ZnQ guest contribution at 371 nm, indicative of the confinement of neat ZnQ^[19] inside the OX-1 pores. Compared to DMF, because DMA is a relatively bulkier molecule, its coordination to the Zn center of ZnQ at two axial positions (Figure 2e inset) might be misplaced upon pore confinement, implicated by caging in the spatially constrained channels (Figure 3). Neat ZnQ complex thus confers extra degrees of freedom to the coordinated bis-8-hydroxyquinoline (8HQ) aromatic moieties around the Zn^{2+} center of the guest emitter; this effect is illustrated in the inset

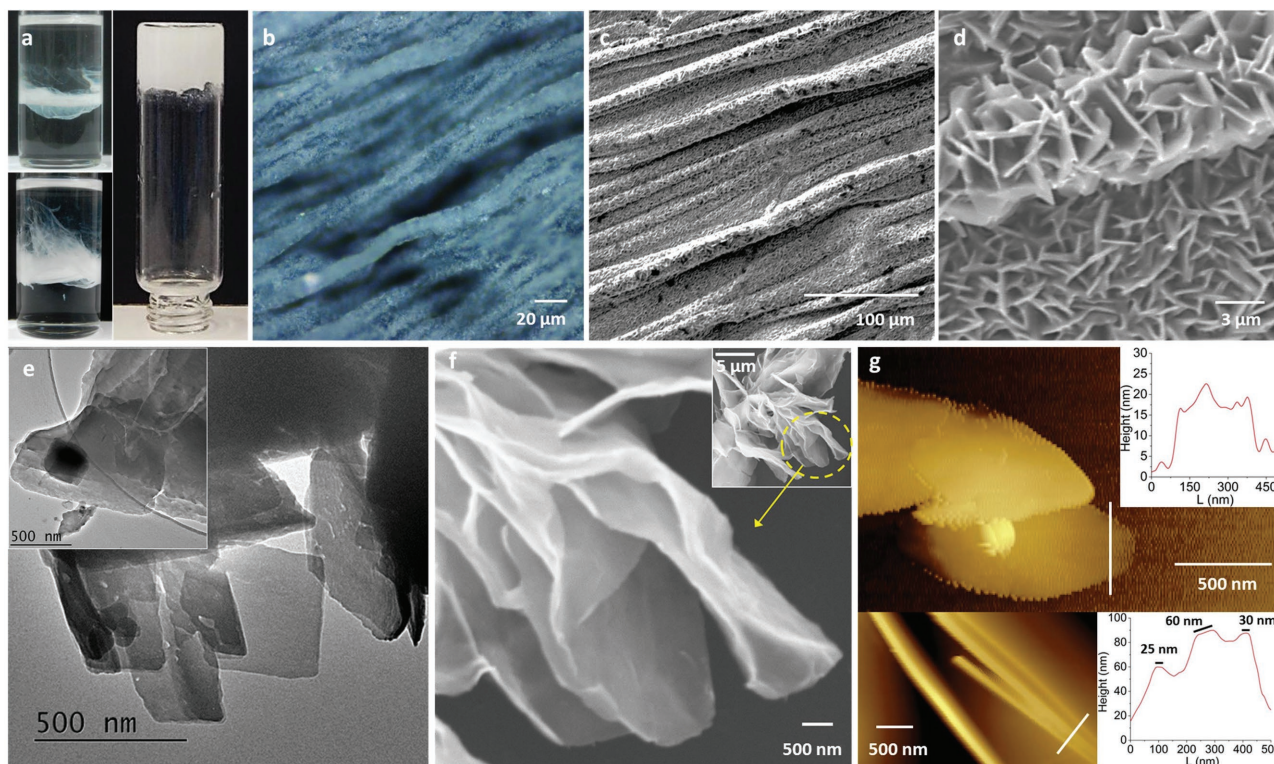


Figure 1. Nanosheets of self-assembled OX-1 MOF materials. a) Supramolecular synthesis showing stepwise development of fibrous soft matter (left), forming a bulk of hybrid gel material (right: confirmed by vial inversion test). b) Optical microscopy image of highly oriented fibrous material revealing shiny fiber surfaces. c) SEM images of aligned fiber microstructures, and d) densely packed nanosheets on gel fibers connected by weak intermolecular interactions. Samples (b)–(d) were synthesized by layering reactant solutions onto a flat glass substrate. e) TEM images of thin 2D morphologies of the exfoliated OX-1 nanosheets; the inset shows similar morphology of functionalized (guest@host) nanosheets of $\text{ZnQ}_{\text{DMF}}@OX-1$. f) SEM image of $\text{ZnQ}_{\text{DMF}}@OX-1$ nanosheets revealing the dissociated 2D layers (this image is a magnified view of the inset microscopy image). g) AFM height topography showing the thickness of the exfoliated layers.

of Figure 2e. In contrast, because Zn metal centers strongly prefer DMF over DMA,^[20] coordinated DMF helps to stabilize the ZnQ structure. This is in agreement with the absorption data of $\text{ZnQ}_{\text{DMF}}@OX-1$ nanosheets, where λ_{max} was pinpointed at 387 nm indicating that the ZnQ has coordinated DMF.

Utilizing Raman vibrational spectroscopy (Figure 2g), we achieved further insights into symmetry alterations of the ZnQ guest emitter as affected by pore confinement. For $\text{ZnQ}_{\text{DMA}}@OX-1$, the doubly degenerate Raman modes at 503.8 cm^{-1} (assigned to skeletal in-plane bending vibrations^[21]) and 514.04 cm^{-1} (Figure S18, Supporting Information) are pointing toward a reduction in molecular symmetry of the neat ZnQ (i.e., without DMA coordination, see Figure 2e inset); this phenomenon is also prominent in pure ZnQ. Interestingly for $\text{ZnQ}_{\text{DMF}}@OX-1$, only a single band was identified at 507.9 cm^{-1} , which meant that the confined ZnQ guest (with DMF) has higher structural symmetry. Relative mode intensities at 740.42 cm^{-1} associated with aromatic ring deformation is appreciably higher in $\text{ZnQ}_{\text{DMA}}@OX-1$ compared to $\text{ZnQ}_{\text{DMF}}@OX-1$, further supporting the notion that the former nanosheet confines neat ZnQ (higher degrees of freedom). The band at 862.5 cm^{-1} corresponds to the out-of-plane $\gamma(\text{C-H})$ bending mode of BDC molecules^[22] in the host framework. For $\text{ZnQ}_{\text{DMF}}@OX-1$, this mode is accompanied by a doubly degenerate band identified at a lower frequency of 852.2 cm^{-1} (Figure S18, Supporting Information), implicated

by strong intermolecular interactions of host–guest aromatic rings hence lessening the structural symmetry.

We measured the fluorescence quantum yield (QY%) of pure ZnQ guest emitter in DMF suspension (35%) and found that, it has risen to 43.8% upon nanoconfinement in the $\text{ZnQ}_{\text{DMF}}@OX-1$ system, which further results in an improved emission lifetime (Figure S19, Supporting Information). Conversely, QY of the $\text{ZnQ}_{\text{DMA}}@OX-1$ system deteriorated to 23.3% (compared to 33% for pure ZnQ in a DMA suspension, see Figure S19, Supporting Information). Our findings are in line with the reported photophysical phenomena where ground and excited states of metal complexes can be modified by fine structural changes from pressure effects, which are manifested as decreasing nonradiative or increasing radiative rates.^[23] Our data suggest that ZnQ caged inside $\text{ZnQ}_{\text{DMF}}@OX-1$ is experiencing compressive strains enhancing its luminescence emission; but $\text{ZnQ}_{\text{DMA}}@OX-1$ is showing a reduction in luminescence due to higher intermolecular interactions between neat ZnQ aromatic rings and the host framework. This reasoning is consistent with the UV–vis and Raman spectroscopic data discussed above.

Our experimental results are further supported by theoretical calculations (see Section 10, Supporting Information), elucidating that the ZnQ guest molecule could adopt different geometrical configurations under pore confinement. Figure 3a shows the optimized structure of ZnQ with two

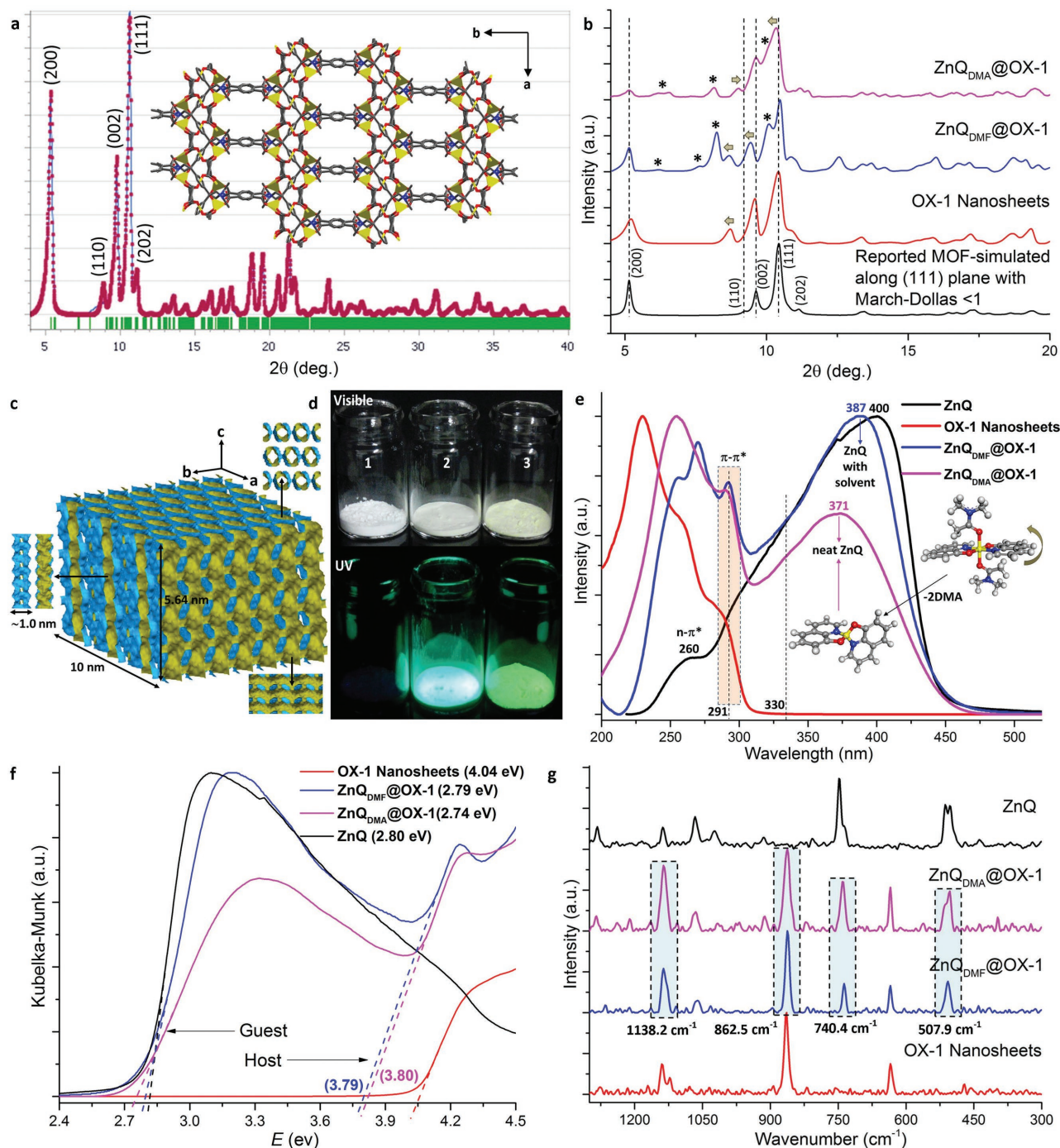


Figure 2. Structural and spectroscopic characterization of the OX-1 nanosheets and their functionalized guest@OX-1 counterparts. a) Pawley refinement^[17] of the OX-1 crystal structure incorporating NEt_3^+ charge-balancing cations ($R_{wp} = 0.084$), and crystallographic view along the c -axis showing 1D porosity (inset). Color scheme: zinc in yellow, nitrogen in blue, oxygen in red, carbon in gray, and hydrogen in white. The traces indicate data as follows: red: experimental data, blue: calculated from structural refinement, and green: observed Bragg peak positions. b) PXRD of nanosheets, with and without confinement of the ZnQ guest molecules, compared with the simulated diffraction pattern from ref. [15] Asterisks mark the positions of the ZnQ peaks. c) Undulating pore architecture of 1D channels along c -axis, solvent accessible volume is denoted by yellow surfaces. d) Emission tests under 365 nm UV irradiation, for sample 1: pristine OX-1 nanosheets without ZnQ is nonemissive; 2: $\text{ZnQ}_{\text{DMF}}@OX-1$; and 3: $\text{ZnQ}_{\text{DMA}}@OX-1$, are optically active. e) UV-vis electronic absorption spectra of the OX-1 host framework, ZnQ guest emitter, and guest@OX-1 composite systems. Inset depicts conformational changes of the neat ZnQ guest emitter molecule, after losing two DMA coordinated solvent molecules from its axial positions. f) Band gap values determined from diffuse reflectance spectra and photon energy intercepts, signifying host-guest interactions. g) Raman spectra revealing intensity and peak alterations arising from the host-guest confinement effects.

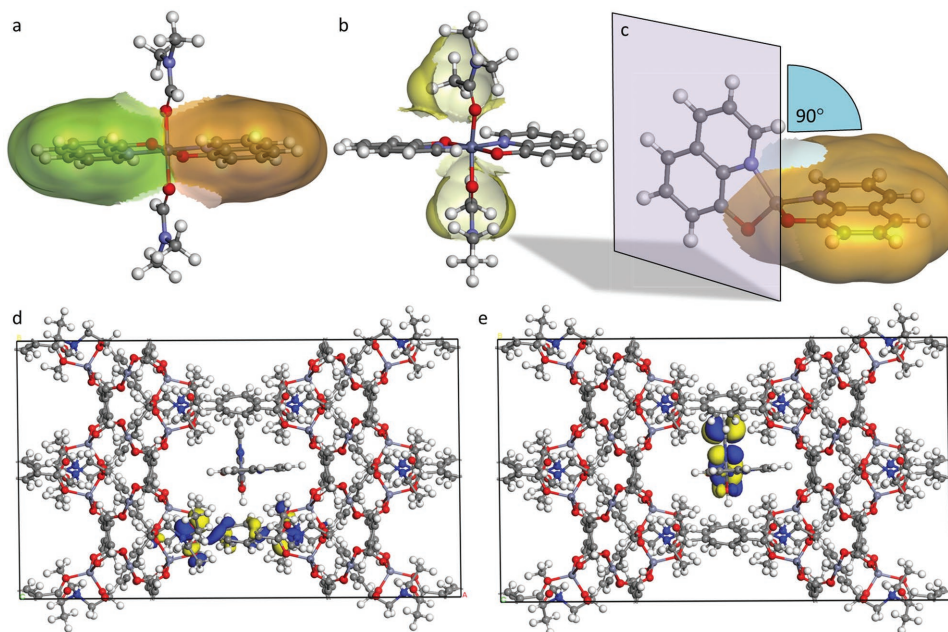


Figure 3. Theoretical determination of the guest molecular structure and electronic orbitals associated with host-guest interactions. Optimized geometries of the ZnQ guest in three different structural configurations: a) DMF solvent molecules coordinated axially to the Zn^{2+} octahedral center; less steric DMF molecule allowing planar spatial arrangement of the 8HQ aromatic rings (indicated by green and orange van der Waals surfaces). b) Steric hindrance from axially coordinated DMA solvent molecules deforming the planarity of 8HQ aromatic rings; yellow surfaces represent CH_3 groups of the coordinated DMA. c) Tetrahedral (Td) configuration achieved upon removal of the two axially coordinated DMA molecules, permitting a 90° rotation of one of the two 8HQ aromatic planes. ZnQ(Td)@OX-1 assembly in which d) HOMO located on the BDC linker of the host framework, while e) LUMO on the aromatic rings of ZnQ guest molecule confined within OX-1 pore. Blue and yellow isosurfaces are positive and negative charges, respectively; see further details in the Supporting Information.

DMF molecules coordinated to the Zn^{2+} axial positions, where the adjacent 8HQ aromatic rings are planar. However, these rings became nonplanar when DMF was substituted by the bulkier DMA molecules (Figure 3b), leading to a significant geometrical distortion in confinement of the OX-1 framework (Figure S21, Supporting Information); such a host-guest configuration is not favorable. In fact, our calculations revealed that ZnQ guest with tetrahedral center (Td) has the preferred geometry (Figure 3c: without coordinated DMA) formed by a 90° rotation of the 8HQ aromatic plane; this configuration also offers good interactions with the host framework via π - π and hydrogen bonding (Figure S23, Supporting Information).

Density functional theory (DFT) band gap calculations show that, for example, when considering ZnQ(Td)@OX-1 pore confinement (Figure 3d,e) the highest occupied molecular orbital (HOMO) is localized on the BDC ring of the OX-1 host, whereas the lowest unoccupied molecular orbital (LUMO) is located on the aromatic rings of the ZnQ molecule. This HOMO-LUMO configuration suggests that host-guest energy transfer will be favorable during photoexcitation of the guest@host assembly. Detailed modifications of the electronic energy levels as a consequence of ZnQ guest confinement in the pore of the OX-1 host are summarized in Figure S24 (Supporting Information), and their HOMO-LUMO frontier orbitals are presented in Table S2 (Supporting Information). It can be seen that the hybrid orbitals of the ZnQ(Td)@OX-1 and ZnQ_{DMF}@OX-1 systems are exhibiting a notable reduction in band gap energies, relative to the isolated OX-1 host and pure ZnQ guest molecule. Our results further

support the recent literature where it has been proposed that: (i) mechanical deformation of flexible MOF structures could produce significant band gap changes^[24] and (ii) localized electronic density distribution of an encapsulated host-guest assembly could enable efficient energy transfer during excitation process.^[25]

We harnessed the tunable luminescent properties of the functionalized guest@OX-1 nanosheets as photoactive materials, accomplishing optochemical sensing of volatile organic compounds (VOCs). Figure 4a and Figure S26 (Supporting Information) show the luminescence data of ZnQ_{DMF}@OX-1 nanosheets as solution-state dispersions, upon perturbation by a series of main solvent species used as analytes. We discover major photophysical response not only in characteristic fluorescence wavelength and intensity (Figure 4b), but also in terms of color chromaticity tuning behavior (Figure 4c). Between the small aliphatic alcohols we probed, methanol caused a fully diminished fluorescence intensity (quenching) after 3–4 min exposure, while nanosheets in isopropanol (IPA) retained majority of its intensity. In fact with rising alcohol polarity (Figure S27, Supporting Information), we observed a sharper decline in emission intensity and a higher frequency red shift following the sequence of: methanol (510 nm) > ethanol (504 nm) > IPA (501 nm). Strongly polarizable protic solvent destabilizes the ZnQ emitter guests, leading to fluorescence quenching via protonation of coordinated oxygen in 8HQ linkers.^[26] Our data indicate excited-state proton-induced charge transfer of ZnQ guests in protic solvents,^[27] where such a mechanism depresses luminescence. The optochemical

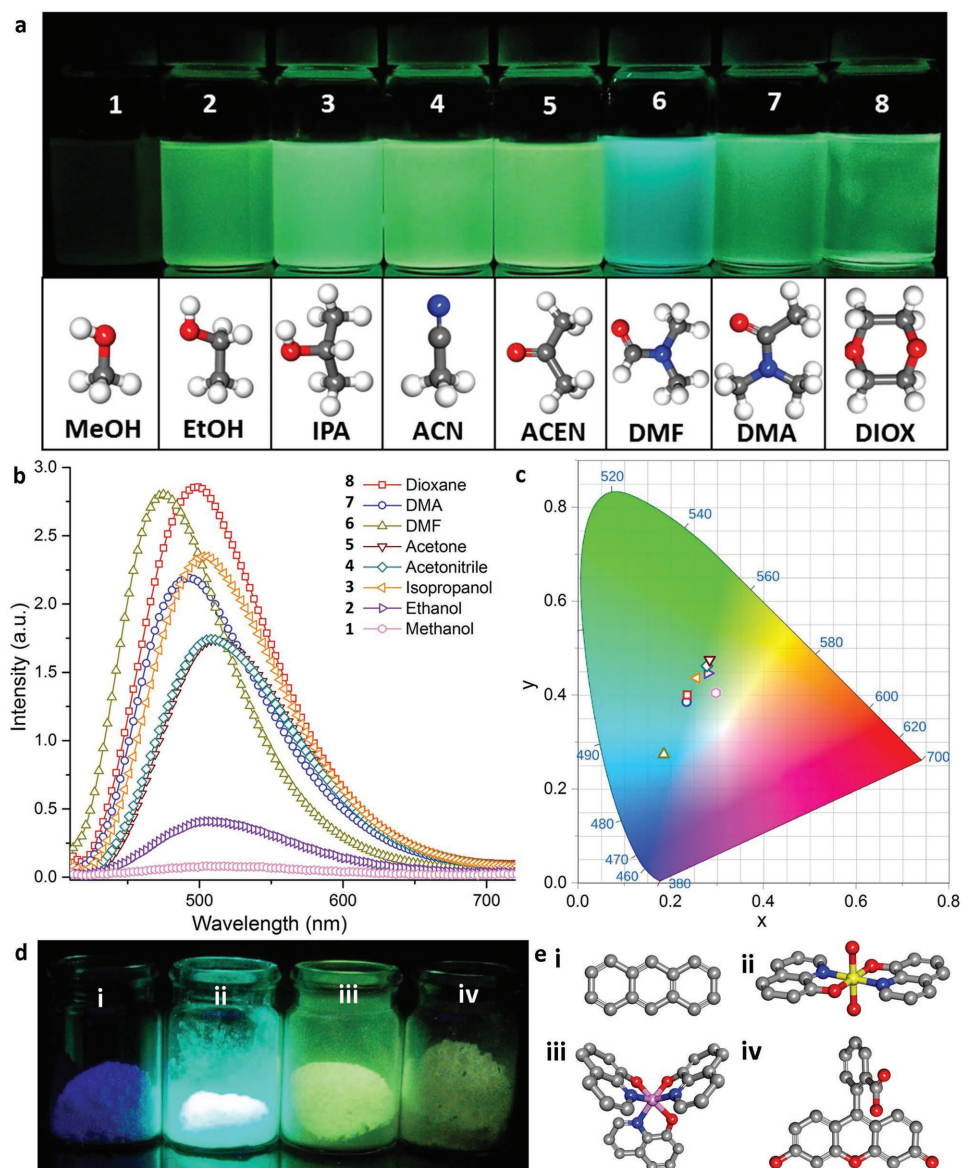


Figure 4. Tunable optochemical behavior of $\text{ZnQ}_{\text{DMF}}@OX-1$ nanosheets. a) Visible to naked eye are distinct modulations in emission properties of dispersions of functionalized nanosheets in a range of small-molecule solvents (each comprising 5 mg of active material in 15 mL solvent). b) Emission profiles and emission intensities of respective dispersions showing different levels of blue (hypsochromic) or red (bathochromic) shifts. c) Chromaticity plot (CIE 1931) indicating the emission color coordinates of the respective dispersions. d) A family of luminescent host-guest materials synthesized by one-pot supramolecular method (Scheme 1), adopting the same OX-1 host framework but confining different e) light-emitting guest molecules: 1: anthracene, 2: ZnQ, 3: AlQ [Al-(tris-8-hydroxyquinoline)], and 4: fluorescein. Color scheme: zinc in yellow, aluminum in pink, nitrogen in blue, oxygen in red, carbon in gray, and hydrogen in white.

sensing results collected from a systematic study of 14 example solvent molecules and VOCs are summarized in Figures S26 and S27 (Supporting Information).

Functionalized nanosheets exposed to nonpolar aliphatic long-chain alkane (*n*-hexane) and cyclic alkane (cyclohexane) displayed interesting optochemical stimulation behaviors. Samples of $\text{ZnQ}_{\text{DMF}}@OX-1$ ($\lambda_{\text{em}} = 470$ nm) dispersed in these aliphatic analytes produced similar fluorescence intensities, but peaked at very different characteristic wavelengths ($\lambda_{\text{em}(n\text{-hexane})} = 496$ nm vs $\lambda_{\text{em}(\text{cyclohexane})} = 477$ nm, see Figure S26, Supporting Information). This meant that higher

molecular mobility of linear *n*-hexane in the OX-1 pores generates a stronger red shift, which can be used to distinguish against the bulkier cyclohexane analyte. Indeed, molecular-size selectivity effect was best demonstrated for the aromatic pair—benzene versus toluene (both of similar polarity), where nanosheets exposed to bulkier toluene experienced only a minor intensity rise, however that caused by benzene was the most intense detected among all the analytes we tested (Figure S26, Supporting Information). Significantly this result elucidates that by increasing π - π interaction within the $\text{ZnQ}_{\text{DMF}}@OX-1$ system, it strengthens fluorescence intensity without modifying

the emission wavelength. Considering yet another pair of related analytes—dichloromethane (DCM) versus chloroform, we established that the relatively smaller DCM molecules can readily infiltrate the tortuous 1D MOF channels (Figure 2c) yielding a major red shift (>30 nm), while diminishing fluorescence intensity due to its strong electron withdrawing nature. Collectively, our comprehensive perturbation data confirmed that the functionalized nanosheets are extremely sensitive toward salient solvent parameters (Figure S27, Supporting Information), encompassing polarity, molecular size, hydrogen bond donor and acceptor affinity, and noncovalent π - π interactions. Long-range crystallinity of the OX-1 host implies that there is a well-ordered arrangement of functional guests (e.g., ZnQ emitters), where its periodicity and accessible porosity (Figure S25, Supporting Information) offer direct interaction with incoming solvent analytes permitting fast chemical detection. In fact, we must recognize that analyte-dependent sensing capability is absent when deploying pure ZnQ complexes alone (Figure S28, Supporting Information), that is, without the host-guest nanoconfinement environment imparted by the porous OX-1 nanosheets.

Motivated by the capacity exhibited by functionalized guest@OX-1 nanosheets in the detection of numerous solvent analytes and VOCs, we present a simple proof-of-concept device

demonstrating the efficacy of ZnQ_{DMF}@OX-1 as a reversible solid-state chemical sensor. A paper-based device (Figure 5a) was fabricated by drop-coating a small amount of ZnQ_{DMF}@OX-1 (e.g., ≈ 2 μ L dispersion made from 5 mg nanosheets suspended in 1 mL hexane) onto a Whatman filter paper. We tested this paper device with a small concentration of analyte. For example, ≈ 1 μ L acetone applied to this paper device swiftly produced a substantial 31 nm red shift (under 365 nm UV), which is clearly perceptible to the naked eye (Figure 5a). Intriguingly, this transition is reversible (507 \rightleftharpoons 476 nm, Figure 5b); the device is again reusable after ≈ 10 s drying time at room temperature as acetone is volatile (in contrast we note that ZnQ_{DMA}@OX-1 has an initial emission wavelength of $\lambda_{em} = 510$ nm, thus rendering it unsuitable for wavelength-shift-based sensing of acetone). Nonetheless, we found that repetitive exposures to acetone could retain the device emission at a higher wavelength of 507 nm. This finding suggests that increased acetone occupancy in OX-1 pores is strengthening noncovalent interactions bridging the ZnQ emitter to the host framework. However, even such an effect is nonpermanent in nature; it can be reverted to its initial 476 nm (blue) emission simply by exposing the device to DMF for several minutes. Key observations made in emission response upon DMF exposure let us elucidate the plausible host-guest interaction mechanisms,

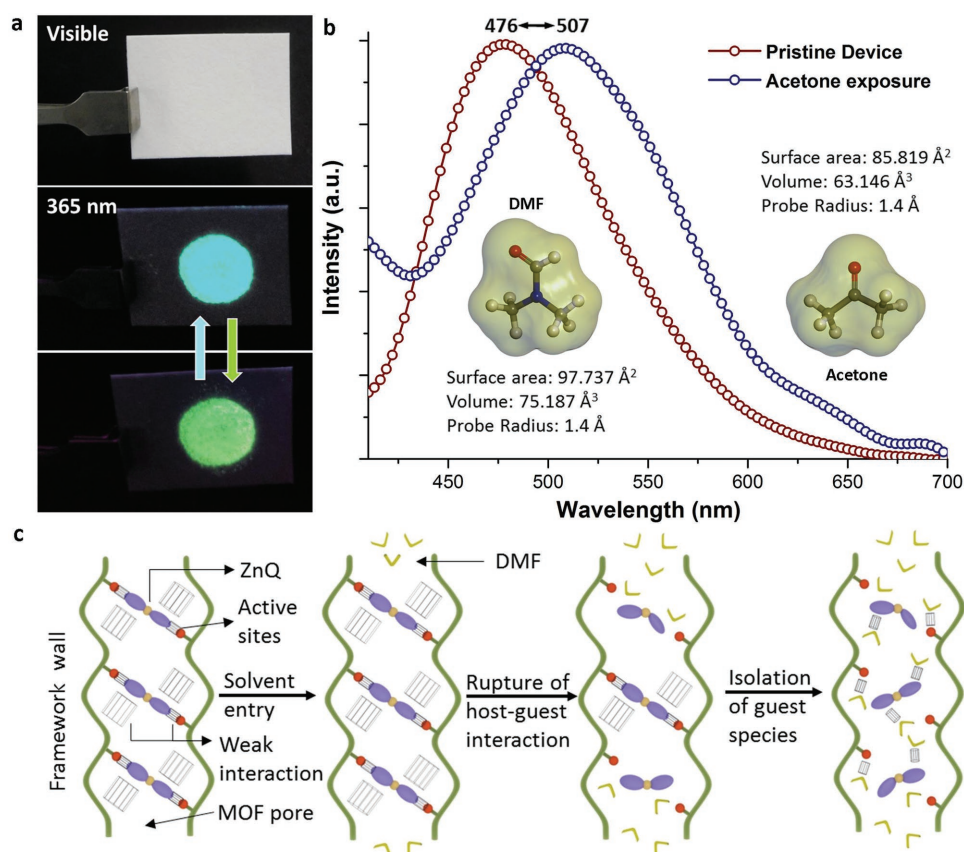


Figure 5. Optochemically active sensory materials comprising ZnQ_{DMF}@OX-1 nanosheets. a) Paper-based optochemical sensor demonstrating reversible acetone sensing ability. b) A 31 nm red shift upon acetone exposure and recovery to its original emission wavelength upon DMF exposure. Inset shows chemical structures of DMF and acetone analytes and their differential molecular sizes. c) Proposed mechanisms involving multiple host-guest interactions under the nanoscale confinement of 1D undulating (tortuous) channels of the OX-1 host framework (vertical: *c*-axis, corresponding to the 1D channels in Figure 2c), and upon the introduction of a DMF analyte triggering a blue shift transformation.

as depicted in Figure 5c. The moment the active material was exposed to DMF, it was observed that emission color quickly turned greenish-yellow for fraction of a second before beginning to undergo blue shifting and eventually returning to its original 476 nm. On this basis, we hypothesize that weak interactions connecting the ZnQ guest and the host framework sites began to slowly rupture upon infiltration of external DMF analyte. We reasoned that penetration of DMF molecules through the 1D tortuous pore channels of the OX-1 host is relatively sluggish, thereby isolating ZnQ from adjacent weak interactions in a stepwise fashion (Figure 5c); eventually this reaches a complete conversion evidenced by the (blue) 476 nm emission. Comparatively immediate response toward acetone exposure can be explained by contrasting the molecular size of the analytes concerned (Figure 5b inset): acetone molecule is $\approx 16\%$ smaller compared to DMF, so the former infiltrates the undulating pores much easier given its smaller size and weakly interacting nature.

In summary, we have elucidated a new paradigm to prepare guest@MOF porous nanosheets, resulting in tunable nanoscale material systems highly sensitive to coupled optoelectronic and chemical perturbations. The proposed HCR supramolecular strategy is very powerful, and it could be utilized to systematically engineer a variety of functionalized guest@MOF composite systems. To show that this is an exciting possibility, we have implemented the HCR approach in conjunction with the guest@OX-1 platform to integrate a number of topical guest emitters successfully (see Figure 4d,e), including anthracene, ZnQ, AlQ [Al-(tris-8-hydroxyquinoline)], naphthalene, and fluorescein.^[14] In the light of this, we anticipate that the proposed methodology will open the door to a new family of low-dimensional MOF-based smart materials, whose bespoke physicochemical properties will be of significant utility to the chemical sensors, photonics, and electronics material sectors.

Experimental Section

Synthesis of Porous OX-1 2D Nanosheets as Host Framework Material: 2 mL DMF clear solution of $\text{Zn}(\text{NO}_3)_2$ (1.5 mmol, termed solution A) was combined with 3 mL clear solution of BDC (3 mmol) plus NEt_3^+ (6 mmol) (termed solution B). A fibrous gel-like supramolecular material formed immediately upon combining solutions A and B. The gel phase is disordered, comprising both crystalline (2D nanosheets) and noncrystalline materials (Scheme 1c) in addition to excess amounts of reactants and guest molecules. The nanosheet-rich fibers were washed twice with copious amounts of polar solvents: first, using DMF followed by methanol and acetone, and with simultaneous sonication (10 min per solvent, then centrifugation). This washing procedure quickly breaks down the supramolecular fibers to release the 2D nanosheets (insoluble), and at the same time removing externally adhered guest species (not in MOF pores) and excess reactants. Finally, nanosheets harvested can be separated by centrifugation (8000 rpm) and subject to vacuum drying at 110 °C for 4 h. The isolated nanosheets are highly crystalline MOF material: $(\text{HNEt}_3)_2[\text{Zn}_3\text{BDC}_4]\cdot\text{DMF}$, designated as “OX-1” nanosheets.

Synthesis of Functionalized MOF Nanosheets of $\text{ZnQ}_{\text{DMF}}@OX-1$ and $\text{ZnQ}_{\text{DMA}}@OX-1$: Preparation of functionalized MOF nanosheet materials (guest@OX-1) involves a simple additional step of in situ mixing of *N,N*-dimethylformamide (as a clear solution) containing the desired guest species (e.g., ZnQ/AlQ/naphthalene/anthracene/fluorescein) into solution B, see Section 1.2 in the Supporting Information for details. The procedures for isolating, washing, and harvesting nanosheets are identical to those described in the foregoing section.

Materials Characterization: The fiber architecture of supramolecular MOF material was confirmed using optical microscopy (Alicona Infinite Focus 3D microscope) and SEM (Carl Zeiss EVO LS15). Detailed nanosheet structures and morphologies were examined under SEM and TEM (JEOL JEM-2100 LaB6, 200 kV), and AFM (Veeco Dimension 3100). Kubelka–Munk (K–M) function was derived from diffuse reflectance spectra measured by UV-2600 UV-vis spectrophotometer, Shimadzu. Steady-state emission spectra and CIE 1931 were recorded using UPRtek spectrophotometer (MK350N Plus). Raman spectroscopy was performed using MultiRAM FT-Raman Spectrometer (Bruker) equipped with a 532 nm laser. PXRD pattern was recorded using the Rigaku MiniFlex with a Cu $K\alpha$ source (1.541 Å), where diffraction data were collected at 2θ angle from 2° to 30°, using a 0.01° step size and 1° min⁻¹ step speed. Quantum yield and fluorescence lifetime measurements were performed on Quantaaurus-QY Absolute PL quantum yield spectrometer (C11347) and Quantaaurus-Tau fluorescence lifetime spectrometer (C11367), respectively. Diluted nanosheet dispersions in respective solvents were used for fluorescence QY and lifetime measurements.

Supporting Information

Supporting Information is available from the Wiley Online Library or from the author. Additional data can be accessed via the Oxford University Research Archive ORA (<http://ora.ouls.ox.ac.uk>).

Acknowledgements

This research was funded by the Samsung Advanced Institute of Technology (SAIT) GRO, the Royal Society Research Grant (RG140296), and the Engineering and Physical Sciences Research Council, EPSRC RCUK (EP/N014960/1 and EP/K031503/1). The authors thank the Research Complex at Harwell (RCaH), Oxfordshire, for access to advanced materials characterization suite. The authors are grateful to Dr. Gavin Stenning and Dr. Marek Jura (R53 Materials Characterization Lab) at the ISIS Rutherford Appleton Laboratory, for provision of X-ray diffraction facilities. The authors acknowledge Dr. James Taylor (R79 Hydrogen and Catalysis Laboratory at ISIS) for performing the BET measurements. The authors thank Dr. M. J. Abdin from Hamamatsu Photonics Ltd. for the provision of quantum yield and fluorescence lifetime spectrometers. Author contributions: A.K.C. and J.C.T. designed the research. A.K.C. performed the experiments and analyzed the data guided by J.C.T. H.J.K. and I.T.H. contributed to the quantum yield measurements and technical insights into sensor device applications. A.K.C. and J.C.T. wrote the paper, with input from all authors.

Conflict of Interest

The authors declare no conflict of interest.

Keywords

host–guest interactions, hybrid materials, metal–organic framework (MOF), nanosheets, photochemical sensors

Received: March 15, 2017
Published online: May 10, 2017

[1] a) H. L. Peng, W. H. Dang, J. Cao, Y. L. Chen, W. Wu, W. S. Zheng, H. Li, Z. X. Shen, Z. F. Liu, *Nat. Chem.* **2012**, *4*, 281; b) M. Osada, T. Sasaki, *Adv. Mater.* **2012**, *24*, 210.

- [2] a) J. Choi, H. Y. Zhang, J. H. Choi, *ACS Nano* **2016**, *10*, 1671; b) J. N. Coleman, M. Lotya, A. O'Neill, S. D. Bergin, P. J. King, U. Khan, K. Young, A. Gaucher, S. De, R. J. Smith, I. V. Shvets, S. K. Arora, G. Stanton, H. Y. Kim, K. Lee, G. T. Kim, G. S. Duesberg, T. Hallam, J. J. Boland, J. J. Wang, J. F. Donegan, J. C. Grunlan, G. Moriarty, A. Shmeliov, R. J. Nicholls, J. M. Perkins, E. M. Grieveson, K. Theuwissen, D. W. McComb, P. D. Nellist, V. Nicolosi, *Science* **2011**, *331*, 568; c) J. C. Tan, P. J. Saines, E. G. Bithell, A. K. Cheetham, *ACS Nano* **2012**, *6*, 615.
- [3] a) Y. Peng, Y. S. Li, Y. J. Ban, H. Jin, W. M. Jiao, X. L. Liu, W. S. Yang, *Science* **2014**, *346*, 1356; b) K. Varoon, X. Zhang, B. Elyassi, D. D. Brewer, M. Gettel, S. Kumar, J. A. Lee, S. Maheshwari, A. Mittal, C. Y. Sung, M. Cococcioni, L. F. Francis, A. V. McCormick, K. A. Mkhoyan, M. Tsapatsis, *Science* **2011**, *334*, 72.
- [4] A. C. Ferrari, F. Bonaccorso, V. Fal'ko, K. S. Novoselov, S. Roche, P. Boggild, S. Borini, F. H. Koppens, V. Palermo, N. Pugno, J. A. Garrido, R. Sordan, A. Bianco, L. Ballerini, M. Prato, E. Lidorikis, J. Kivioja, C. Marinelli, T. Ryhanen, A. Morpurgo, J. N. Coleman, V. Nicolosi, L. Colombo, A. Fert, M. Garcia-Hernandez, A. Bachtold, G. F. Schneider, F. Guinea, C. Dekker, M. Barbone, Z. Sun, C. Galiotis, A. N. Grigorenko, G. Konstantatos, A. Kis, M. Katsnelson, L. Vandersypen, A. Loiseau, V. Morandi, D. Neumaier, E. Treossi, V. Pellegrini, M. Polini, A. Tredicucci, G. M. Williams, B. H. Hong, J. H. Ahn, J. M. Kim, H. Zirath, B. J. van Wees, H. van der Zant, L. Occhipinti, A. Di Matteo, I. A. Kinloch, T. Seyller, E. Quesnel, X. Feng, K. Teo, N. Rupesinghe, P. Hakonen, S. R. Neil, Q. Tannock, T. Lofwander, J. Kinaret, *Nanoscale* **2015**, *7*, 4598.
- [5] a) J. M. Lehn, *Proc. Natl. Acad. Sci. USA* **2002**, *99*, 4763; b) E. R. Draper, E. G. B. Eden, T. O. McDonald, D. J. Adams, *Nat. Chem.* **2015**, *7*, 849.
- [6] B. Choi, J. Yu, D. W. Paley, M. T. Trinh, M. V. Paley, J. M. Karch, A. C. Crowther, C. H. Lee, R. A. Lalancette, X. Y. Zhu, P. Kim, M. L. Steigerwald, C. Nuckolls, X. Roy, *Nano Lett.* **2016**, *16*, 1445.
- [7] a) G. Xu, T. Yamada, K. Otsubo, S. Sakaida, H. Kitagawa, *J. Am. Chem. Soc.* **2012**, *134*, 16524; b) Y. Sakata, S. Furukawa, M. Kondo, K. Hirai, N. Horike, Y. Takashima, H. Uehara, N. Louvain, M. Meilikhov, T. Tsuruoka, S. Isoda, W. Kosaka, O. Sakata, S. Kitagawa, *Science* **2013**, *339*, 193; c) M. Zhao, Y. Wang, Q. Ma, Y. Huang, X. Zhang, J. Ping, Z. Zhang, Q. Lu, Y. Yu, H. Xu, Y. Zhao, H. Zhang, *Adv. Mater.* **2015**, *27*, 7372; d) T. Rodenas, I. Luz, G. Prieto, B. Seoane, H. Miro, A. Corma, F. Kapteijn, I. X. F. X. Llabres, J. Gascon, *Nat. Mater.* **2015**, *14*, 48; e) C. Hermosa, B. R. Horrocks, J. I. Martinez, F. Liscio, J. Gomez-Herrero, F. Zamora, *Chem. Sci.* **2015**, *6*, 2553.
- [8] a) A. J. Howarth, Y. Liu, P. Li, Z. Li, T. C. Wang, J. T. Hupp, O. K. Farha, *Nat. Rev. Mater.* **2016**, *1*, 15018; b) B. Garai, A. Mallick, R. Banerjee, *Chem. Sci.* **2016**, *7*, 2195; c) M. S. Yao, W. X. Tang, G. E. Wang, B. Nath, G. Xu, *Adv. Mater.* **2016**, *28*, 5229; d) M. R. Ryder, J. C. Tan, *Mater. Sci. Technol.* **2014**, *30*, 1598.
- [9] a) R. Ameloot, F. Vermoortele, W. Vanhove, M. B. J. Roeffaers, B. F. Sels, D. E. De Vos, *Nat. Chem.* **2011**, *3*, 382; b) M. OvKeeffe, O. M. Yaghi, *Chem. Rev.* **2012**, *112*, 675; c) M. R. Ryder, B. Civalieri, G. Cinque, J. C. Tan, *CrystEngComm* **2016**, *18*, 4303.
- [10] a) N. Liedana, A. Galve, C. Rubio, C. Tellez, J. Coronas, *ACS Appl. Mater. Interfaces* **2012**, *4*, 5016; b) R. Anand, F. Borghi, F. Manoli, I. Manet, V. Agostoni, P. Reschiglian, R. Gref, S. Monti, *J. Phys. Chem. B* **2014**, *118*, 8532; c) A. K. Chaudhari, M. R. Ryder, J. C. Tan, *Nanoscale* **2016**, *8*, 6851; d) W. Xie, W. W. He, D. Y. Du, S. L. Li, J. S. Qin, Z. M. Su, C. Y. Sun, Y. Q. Lan, *Chem. Commun.* **2016**, *52*, 3288.
- [11] a) M. D. Allendorf, M. E. Foster, F. Leonard, V. Stavila, P. L. Feng, F. P. Doty, K. Leong, E. Y. Ma, S. R. Johnston, A. A. Talin, *J. Phys. Chem. Lett.* **2015**, *6*, 1182; b) J. Aguilera-Sigalat, D. Bradshaw, *Coord. Chem. Rev.* **2016**, *307*, 267.
- [12] a) L. E. Kreno, K. Leong, O. K. Farha, M. Allendorf, R. P. Van Duyne, J. T. Hupp, *Chem. Rev.* **2012**, *112*, 1105; b) Z. Hu, B. J. Deibert, J. Li, *Chem. Soc. Rev.* **2014**, *43*, 5815.
- [13] A. K. Chaudhari, I. Han, J. C. Tan, *Adv. Mater.* **2015**, *27*, 4438.
- [14] See the Supporting Information—Materials and Methods.
- [15] A. D. Burrows, K. Cassar, R. M. W. Friend, M. F. Mahon, S. P. Rigby, J. E. Warren, *CrystEngComm* **2005**, *7*, 548.
- [16] E. Biemmi, T. Bein, N. Stock, *Solid State Sci.* **2006**, *8*, 363.
- [17] G. S. Pawley, *J. Appl. Crystallogr.* **1981**, *14*, 357.
- [18] L. S. Sapochak, F. E. Benincasa, R. S. Schofield, J. L. Baker, K. K. C. Riccio, D. Fogarty, H. Kohlmann, K. F. Ferris, P. E. Burrows, *J. Am. Chem. Soc.* **2002**, *124*, 6119.
- [19] N. Khaorapapong, M. Ogawa, *J. Phys. Chem. Solids* **2008**, *69*, 941.
- [20] S. Ishiguro, Y. Umeyayashi, R. Kanzaki, *Anal. Sci.* **2004**, *20*, 415.
- [21] V. Krishnakumar, R. Ramasamy, *Spectrochim. Acta A* **2005**, *61*, 673.
- [22] M. W. Lee, M. S. Kim, K. Kim, *J. Mol. Struct.* **1997**, *415*, 93.
- [23] a) R. W. Parsons, H. G. Drickamer, *J. Chem. Phys.* **1958**, *29*, 930; b) J. K. Grey, I. S. Butler, *Coord. Chem. Rev.* **2001**, *219*, 713; c) C. Reber, *Can. J. Anal. Sci.* **2008**, *53*, 91.
- [24] S. Ling, B. Slater, *J. Phys. Chem. C* **2015**, *119*, 16667.
- [25] D. Yan, Y. Tang, H. Lin, D. Wang, *Sci. Rep.* **2014**, *4*, 4337.
- [26] B. Valeur, I. Leray, *Coord. Chem. Rev.* **2000**, *205*, 3.
- [27] E. Bardez, I. Devol, B. Larrey, B. Valeur, *J. Phys. Chem. B* **1997**, *101*, 7786.